Granular collapse on particle-laden water

Nathan Reyner [1], Chase T. Gabbard [2], and Joshua B. Bostwick [1,*]
[1]*Department of Mechanical Engineering, Clemson University, Clemson, South Carolina 29631, USA*
[2]*School of Engineering, Brown University, Providence, Rhode Island 02912, USA*

(Received 17 October 2025; accepted 27 January 2026; published 12 February 2026)

We investigate the generation and propagation of an impulse wave on a particle-laden water bath produced by the subaerial collapse of a granular column. Laboratory experiments were performed by releasing dense granular columns into water covered with a monolayer of buoyant particles. By systematically varying column height, water depth, and particle size, we explored the role of the buoyant particles on wave type and characteristics, and made direct comparisons with waves on a particle-free interface. The coupled particle–wave dynamics were found to markedly reshape both the waveform and the particle distribution. Buoyant particles delayed the transition from nonbreaking to breaking waves, with the magnitude of the delay increasing with particle size. After wave generation, two distinct particle-accumulation regions emerged: a static buildup adjacent to the collapsed grains that buttressed the pile, and a dynamic concentration zone traveling with the wave front that acted to suppress breaking. Despite these differences from the particle-free case, the maximum wave amplitude was found to primarily correlate with the geometry of the collapsed column, enabling the use of a simple model to relate the wave amplitude and initial column configuration. These results suggest that a buoyant surface layer modulates wave generation and propagation, providing potential insights into impulse waves triggered by glacier calving in proglacial fjords laden with ice mélange.

DOI: 10.1103/hcyb-7nhz

I. INTRODUCTION

On December 22, 2018, a deadly tsunami struck the coasts of Java and Sumatra, Indonesia's two largest islands. Unlike most tsunamis, it was not triggered by an earthquake but by the partial collapse of the erupting Anak Krakatau volcano [1]. The catastrophic impact of such events has motivated extensive laboratory studies of tsunami generation, often modeled by submerging dense granular columns into water [2–4]. Although these experiments are many orders of magnitude smaller than real events, they have provided valuable physical insight and yielded predictive models that compare well with field observations [5]. Moreover, they offer a controlled setting to probe the influence of key factors, such as the slope of the subaerial and submarine floor [6,7], and the relative volume of submerged grains [3,8]. These studies, however, typically assume a pristine water–air interface, free of floating debris. This assumption contrasts sharply with present-day conditions: human-driven climate change, plastic pollution, and industrial accidents now blanket fragile ocean regions with freshly calved ice, discarded plastics, and oil slicks. This reality raises urgent questions about how tsunami-generating events, such as the increasingly frequent tsunamis generated from iceberg calving [9,10], are affected by buoyant material coating the surrounding water, such as ice mélange. To address these questions, we introduce a new set of laboratory experiments in

*Contact author: jbostwi@clemson.edu; https://cecas.clemson.edu/~jbostwi/

which granular columns collapse into water covered by buoyant particles, providing a controlled framework to probe the role of floating debris on wave formation and propagation.

Various techniques have been employed to generate surface waves in laboratory settings, including moving a vertical wall [11], translating the bottom boundary [12], driving the water with a rigid piston [13], impacting the surface with a solid body [14–16], capsizing a buoyant object [17], and collapsing a pile of granular material into the water [2]. In modeling landslide-generated waves, collapse events are commonly classified as subaerial, when the material originates above the waterline; submarine, when it begins below the waterline; or partially submerged, for intermediate cases. Subaerial scenarios can be reproduced in the laboratory using granular material, with the initial configuration and properties chosen to reflect the conditions of interest. For example, the dense granular mass may be continuously supplied to avoid finite-volume effects [18] or replaced with buoyant grains to investigate avalanche-generated surface waves [19]. While most of these experiments have been conducted in quasi-2D configurations, fully 3D physical models have also been developed [20] and applied to nonplanar scenarios, such as landslides on a conical hill [7]. In more recent studies, rectangular columns of dry grains have provided a simple initial geometry that provides scaled results similar to those observed in nature [5].

Tsunami generation by granular collapse arises from a competition between gravitational and inertial forces. For a rectangular column of dry grains, this competition may be expressed as a comparison between the vertical velocity of the collapsing grains $\sqrt{2\,g H_0}$ and the phase speed of gravity waves in water $\sqrt{g\,h_0}$, where H_0 and h_0 denote the initial heights of the granular column and water depth, respectively [8]. Their ratio defines a global Froude number,

$$Fr_0 = \sqrt{\frac{H_0}{h_0}}. \tag{1}$$

While Fr_0 captures the relative importance of these scales, Robbe-Saule *et al.* [8] demonstrated that it fails to fully describe the resulting wave amplitude and wavelength, as it neglects geometric factors such as the column aspect ratio. Assuming the horizontal motion of the grains acts like a rigid piston driving the fluid, they introduced a local Froude number,

$$Fr_f = \frac{v_m}{\sqrt{g\,h_0}}, \tag{2}$$

where v_m is the maximum horizontal velocity of the granular front at the waterline. This local Froude, along with a modified version accounting for wave amplitude, was shown to correlate more closely with experimental data. Moreover, Sarlin *et al.* [21] demonstrated that increasing Fr_f drives a sequence of wave-type transitions, from nonlinear transition waves to solitary waves and finally to bore waves, consistent with earlier observations by Fritz *et al.* [22]. Building on this framework, the spreading dynamics of the grains were later used to develop a predictive model for wave amplitude [23]. The piston-like analogy for the horizontal grain motion was further validated by experiments on waves generated through the impulsive motion of a vertical wall, where the observed regimes depend on both the relative stroke length and a piston-defined Froude number [13]. Notably, in all of these studies, the water–air interface was free of floating debris.

In many real-world settings, water surfaces are coated with a variety of debris, including anthropogenic accumulations of plastic waste [24,25] and natural deposits such as pumice rafts [26] and floating ice [27]. A particularly relevant example is ice mélange, a dense matrix of floating ice that often forms ahead of calving glaciers, which has been physically modeled at laboratory scales as a large granular flow, providing an accessible means to investigate its dynamics and stress field [28]. When glacial calving occurs, a brittle mass of ice falls into the water below, often fragmenting into a large number of individual masses [29] and producing large waves upon impact [10,30–32]. Such waves can be used to predict the calving flux, the rate at which ice is lost from the terminus due to calving [9], where the effect of the floating debris on wave generation and propagation is largely ignored. However, many common floating debris such as oil slicks [33], grease ice [34], foam [35],

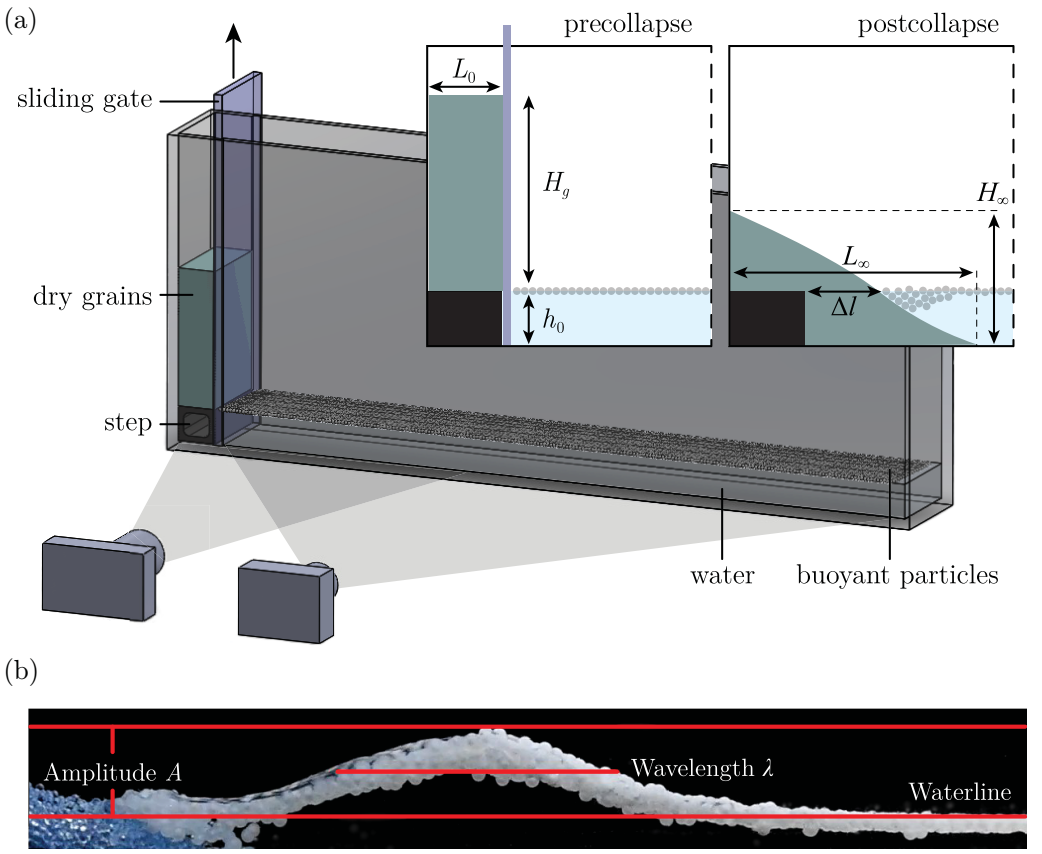

FIG. 1. (a) Schematic of the experimental setup, and annotated illustrations of the pre- and postcollapse configuration. (b) A typical experimental image with measured variables overlaid.

surfactants [36], and buoyant spheres [37] are known to dampen surface disturbances. In particular, closely packed floating spheres can attenuate wave propagation [38], a condition characteristic of ice-choked waters, where complex stress distributions and jamming arise [28,39–41]. Motivated by these findings, the present study introduces new laboratory experiments that examine how buoyant particles on a water surface affect the generation and propagation of impulse waves triggered by granular collapse, with implications for understanding wave generation during iceberg calving [30] and iceberg capsizing events [42,43].

Our article is organized as follows. Section II describes the experiment design and details the experimental procedure. In Sec. III, we describe the typical wave generation process and highlight features unique to particle-laden water. Section IV presents dimensional trends and their dependence on the relevant experimental parameters. We then use scaling arguments to analyze our data and empirical arguments to generate a predictive model for the wave amplitude in Sec. V. In Sec. VI, we contextualize these findings and discuss their broader implications, before concluding in Sec. VII with a summary of key results and potential directions for future work.

II. EXPERIMENT

We conducted laboratory-scale granular collapse experiments using the setup shown in Fig. 1(a). The apparatus is a rectangular tank (length 111 cm, width 13 cm, height 44 cm) divided by a vertically sliding gate guided by machined grooves. One side of the gate contains a bath of

TABLE I. Variable ranges.

Parameter	Symbol	Units (cgs)	Range
Water depth	h_0	cm	1.70–7.95
Buoyant particle radius	R	cm	0.159–0.635
Granular column height	H_g	cm	10–30
Granular column volume	V_g	cm^3	728–2184
Aspect ratio	α		2.63–6.20
Global Froude number	Fr_0		1.77–3.58

room-temperature water of density $\rho_w = 0.998\ g/cm^3$ and height h_0. On the other side, a 3D-printed step of equal height supports a column of dry glass beads with radius $R_g = 2.5\,mm$ and density $\rho_g = 2.214\ g/cm^3$. The apparent volume of the granular column, $V_g = H_0 L_0 W_0$, is controlled by varying the column height H_0, while its length $L_0 = 5.6\,cm$ and width $W_0 = 13\,cm$ remain fixed. At the water–air interface, a monolayer of polypropylene particles with density $\rho = 0.913\ g/cm^3$ and radius R floats with packing fraction $\Phi \approx 0.88$. The explored variable ranges are summarized in Table I.

Each experiment began by placing a step of height h_0 on one side of the tank partition and positioning a 3D-printed grate flush with the tank bottom on the opposite side to minimize slip. To prevent splashing, a monolayer of buoyant particles was first added to the empty tank, after which water was slowly introduced through a bulkhead near the bottom of the tank. Once the water level matched the step height, a stirring rod was used to distribute the particles uniformly across the interface. The sliding gate was then lowered into the partition, and glass beads were gently poured onto the step until the granular column reached the prescribed height H_0. Note that all experiments are conducted with dry glass beads to avoid cohesive effects during the collapse of the granular column [44]. After all motion in both the column and the bath had subsided, the gate was rapidly raised in less than 0.15 s, initiating the collapse of the granular column into the water under gravity. The experiment concluded once all motion within the tank had ceased. Each experiment was repeated at least three times, and the reported values represent the average over those runs, with error bars indicating the 95% confidence interval.

The wave formation and propagation dynamics were recorded using cameras positioned at the waterline. A Chronos high-speed camera equipped with a Venus macro lens captured the collapse region at 600 fps, while a Nikon DSLR with an AF-P Nikkor 18–55 mm lens imaged the full tank length at 60 fps. Figure 1 (a) illustrates the approximate field of view of each camera with gray shading. Two lighting configurations were employed. For experiments with particle-laden water, light sources were placed above and below the tank, with a black background to maximize contrast against the buoyant particles and glass beads. For experiments with a particle-free interface, a light panel was positioned behind the tank, and a small amount of blue dye was added to the water to enhance contrast for image analysis. Wave features were quantified using a custom MATLAB script that isolated the wave (see Appendix) and detected both the waterline and the wave peak. The wave amplitude A was defined as the difference between these two levels, while the half-height wavelength λ, hereafter referred to simply as the wavelength, was defined as the width of the wave at the midpoint between the waterline and the wave peak, as illustrated in Fig. 1 (b). Granular collapse dynamics were tracked along the waterline. The granular front velocity v_g was obtained by tracking the distance from the step front to the farthest glass bead over time, while the total granular runout ΔL_∞ [Fig. 1 (a), inset] corresponded to this same distance measured once all motion had subsided.

III. WAVE GENERATION

Waves generated in pro-glacial fjords by calving events are typically described as impulse waves, analogous to those produced by landslides, and can be modeled at a laboratory scale by the subaerial

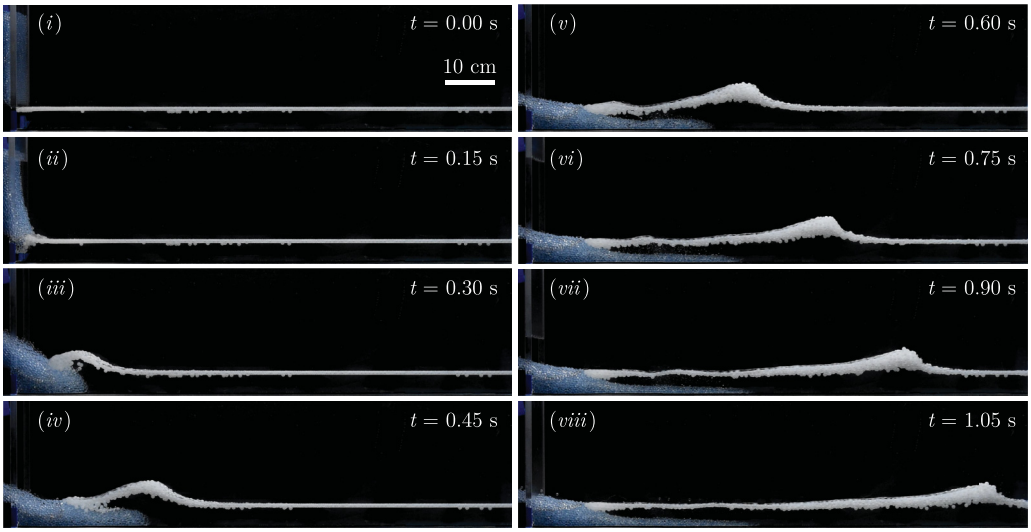

FIG. 2. A granular column of height $H_g = 20\,\text{cm}$ is released onto a water layer $h_0 = 4.7\,\text{cm}$ covered with a monolayer of buoyant particles $R = 3.97\,\text{mm}$.

collapse of granular columns into water. Figure 2 demonstrates such an experiment at select times during wave formation [(i) to (iv)] and propagation [(v) to (viii)]. In this example, the granular column height was $H_g = 20\,\text{cm}$, the water depth $h_0 = 4.7\,\text{cm}$, and the buoyant particle radius $R = 3.97\,\text{mm}$, corresponding to a global Froude number $Fr_0 = 2.3$. After the sliding gate is opened ($t = 0\,\text{s}$), the granular column collapsed into the water under the action of gravity, generating a wave that propagated outward (see [45], Movie 1). During the formation stage [(ii) to (iv)], the wave amplitude and wavelength increased, while the falling granular pile dragged buoyant particles into the water (v). The buoyant particles near the granular front accumulated into a high-density region that persisted even after the wave detached from the granular front. During propagation, the wave profile and particle distribution became skewed: the wave tail elongated and entrained a large number of buoyant particles, while beneath the wave crest, particles traveled with the wave and compressed the monolayer ahead of it. These features may be contrasted with the clean-water case of Robbe-Saule *et al.* [8] (see their Fig. 2). Although the overall wave properties exhibited similar trends during formation, the presence of the buoyant layer introduced two regions of high particle concentration: one localized near the collapsed pile and another dynamic region traveling with the wave. The qualitative influence of the buoyant layer is evident in these regions, motivating a quantitative analysis of its effect on wave properties.

IV. PARTICLE-LADEN WAVES

Granular collapse onto still water produces three distinct wave types that depend on the global Froude number Fr_0 [21]. At small Fr_0, when the granular column height is short relative to the water depth, the grains fall largely vertically through the air–water interface, displacing little water and generating nonlinear transition waves. At large Fr_0, the collapse behaves like a linear piston, driving water outward and producing a bore wave of large amplitude and short wavelength, which may break when the leading-edge slope becomes too steep [21]. Between these two limits, solitary waves form, characterized by a nearly symmetric profile. In the following sections, we concentrate on solitary and bore waves, as nonlinear transition waves typically have amplitudes comparable to the diameter of the buoyant particles.

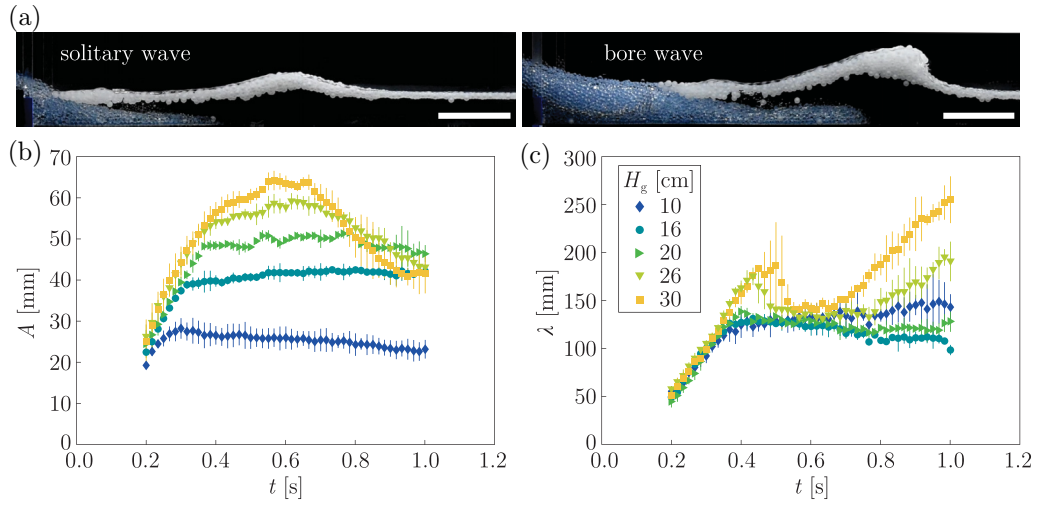

FIG. 3. (a) A solitary wave (left) and a breaking bore wave (right) produced from the collapse of a granular column with height $H_g = 10\,\text{cm}$ and $H_g = 20\,\text{cm}$, respectively. Scale bars are 10 mm long, $h_0 = 4.7\,\text{cm}$ and $R = 3.97\,\text{mm}$. (b) Amplitude A and (c) wavelength λ against time t as it depends upon granular column height H_g. Error bars show 95% confidence intervals.

A. Varying granular column height H_g

Fixing the length and width of the granular column and increasing its height H_g transitions the wave type from solitary to bore. Figure 3(a) shows this transition for an experiment with $H_g = 10\,\text{cm}$ (left) and $H_g = 20\,\text{cm}$ (right), where the water depth $h_0 = 4.7\,\text{cm}$ and $R = 3.97\,\text{mm}$. Notably, the additional granular material increases the horizontal runout, and the wave amplitude is increased. The corresponding movies 2 and 3 are available in [45]. Figure 3(b) shows the wave amplitude A against time t for $h_0 = 4.7\,\text{cm}$ and $R = 3.97\,\text{mm}$, with granular column height H_g increasing from dark blue to light yellow. At the lowest column height, the maximum amplitude is small, reached quickly, and decays gradually as the wave propagates. At intermediate heights, the wave develops into a nonbreaking bore, with faster growth and larger maximum amplitude. These waves then travel across the tank at nearly constant amplitude. The two largest column heights generate breaking bores: they form and grow similarly to nonbreaking bores, but shortly after reaching maximum amplitude, they break and lose energy rapidly. The taller the granular column, the sharper the amplitude drop following breaking. Figure 3(c) shows the wavelength λ against time t for the same experiments. The low-amplitude solitary wave, nonbreaking bore waves, and breaking bore waves have similar growth rates but distinct trends during the propagation phase. Solitary waves slowly spread as they move along the tank, increasing λ slightly over the length of the experiment. In contrast, bore waves narrow slightly. Most interestingly, for breaking bore waves, λ increases during formation, decreases during breaking, and then rises sharply again as the collapsed wave expands.

B. Varying water depth h_0

Figure 4(a) shows the wave amplitude A against time t, as it depends upon the water height h_0, for constant granular column height $H_g = 20\,\text{cm}$ and buoyant particle size $R = 3.97\,\text{mm}$. When the water is shallow, the large horizontal runout of the granular material generates breaking bore waves whose growth during formation is quickly reversed when the wave breaks. At intermediate h_0 (4.70 cm and 5.70 cm), the waves are nonbreaking bore waves that grow to a maximum size at a similar rate and propagate at a nearly constant amplitude. The largest h_0 data corresponds

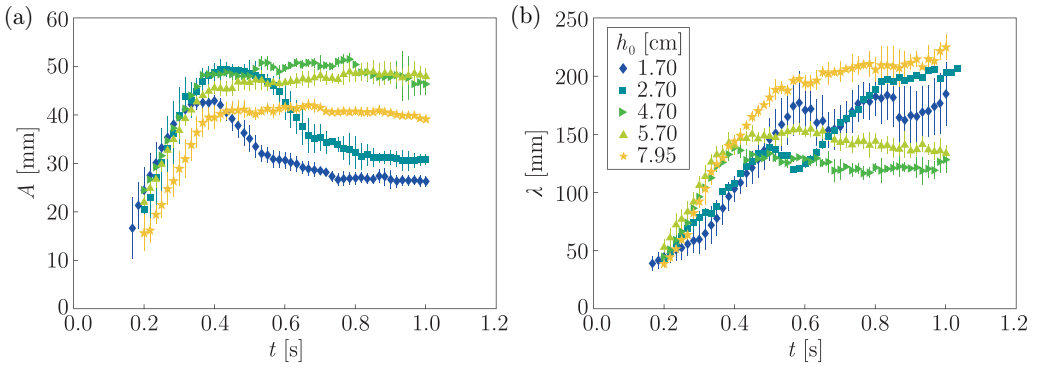

FIG. 4. (a) Amplitude A and (b) wavelength λ against time t as it depends upon water height h_0. Error bars show 95% confidence intervals, $H_g = 20\,\text{cm}$ and $R = 3.97\,\text{mm}$.

to a solitary wave whose growth is slower and stunted relative to the higher energy bore waves, similar to the differences observed between bore and solitary waves as H_g was varied. Unlike those earlier results, however, the maximum amplitude here is nonmonotonic: as h_0 decreases, breaking bores form whose peak amplitude is reduced relative to the nonbreaking cases. This suggests that shallower water enhances the horizontal motion of the grains but suppresses wave amplitude if the depth is too small. Figure 4(b) shows the wavelength λ as a function of time t for the same experiments as in Fig. 4(a). As in the previous subsection, the breaking waves follow three distinct stages: λ increases during formation, decreases as the wave breaks, and then increases again as the wave elongates post-breaking. The two nonbreaking bore waves ($h_0 = 4.70\,\text{cm}$ and 5.70 cm) broaden during formation but gradually decrease in wavelength as they propagate. In contrast, the solitary wave ($h_0 = 7.95\,\text{cm}$) continues to lengthen throughout the propagation phase. These behaviors are consistent across repeated trials and align with the trends reported in the previous subsection.

C. Varying buoyant particle radius *R*

To highlight the strong influence of particle size on wave evolution, we performed a set of experiments near the transition between breaking and nonbreaking bore waves. Figure 5(a) shows

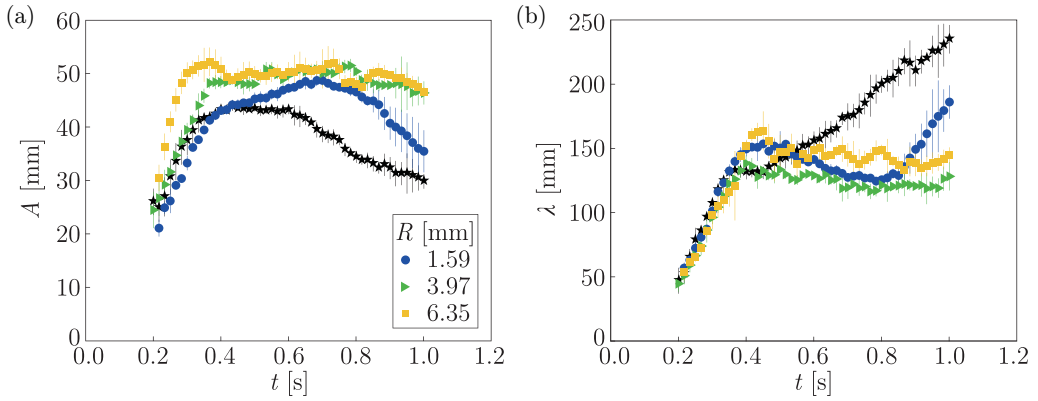

FIG. 5. (a) Amplitude A and (b) wavelength λ against time t as it depends upon buoyant particle radius R. Error bars show 95% confidence intervals, $H_g = 20\,\text{cm}$ and $h_0 = 4.7\,\text{cm}$.

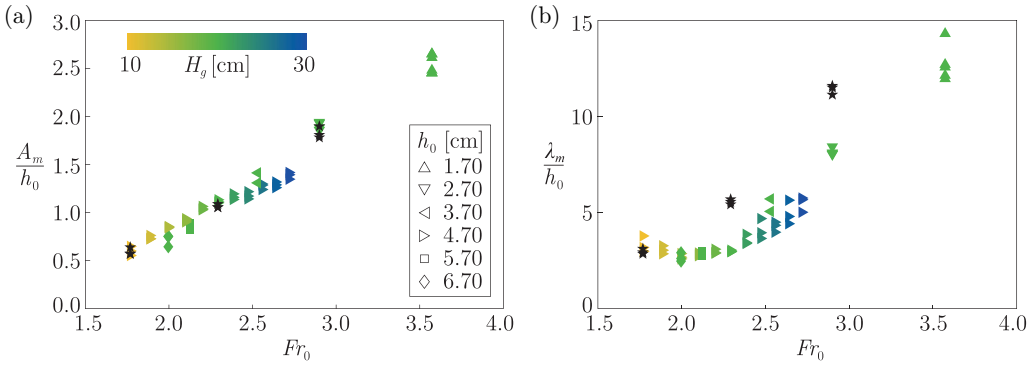

FIG. 6. (a) Dimensionless amplitude A_m/h_0 and (b) wavelength λ/h_0 against global Froude number Fr_0. Marker symbol indicates water depth h_0, and marker color maps to granular column height H_g on a linear scale. Black stars represent experiments using particle-free water.

the wave amplitude A as a function of time t for different particle sizes (colored data) at $H_g = 20\,\text{cm}$ and $h_0 = 4.7\,\text{cm}$. For comparison, a clean water case under the same conditions is shown as black stars. In the particle-free case, the collapse generates a breaking bore wave, with A increasing during formation and then decreasing sharply as the wave breaks. Introducing small particles ($R = 1.59\,\text{mm}$) increases the maximum amplitude and delays wave breaking. As the particle size increases further, the wave transitions from breaking to nonbreaking, with A remaining nearly constant during propagation. Figure 5(b) shows the corresponding wavelength λ over time for the same experiments. The particle-free breaking wave exhibits a rapid increase in λ as it propagates, reflecting the widening of the wave after breaking. The case with $R = 1.59\,\text{mm}$ particles follows the same overall trend but delays the onset of the final wavelength growth stage by roughly a factor of two compared to the clean-water case. For larger particle sizes, the resulting nonbreaking waves display a different behavior: λ increases with t during wave formation but then decreases steadily as the wave travels across the tank.

V. DIMENSIONLESS TRENDS

We now directly compare individual experiments with and without buoyant particles using the global Froude number (1). Figure 6(a) shows the scaled maximum amplitude A_m/h_0 plotted against the global Froude number Fr_0, with marker color indicating H_g and marker shape indicating h_0. Black stars denote particle-free water experiments. At first glance, the data appear strongly correlated; however, contrasting cases with constant $h_0 = 4.7\,\text{cm}$ to those with constant $H_g = 20\,\text{cm}$ reveals that the trends are not parallel. As discussed in Robbe-Saule *et al.* [8] for particle-free water, the global Froude number is insufficient to fully capture the dependence of wave amplitude, particularly when the column aspect ratio varies. This trend is evident in our results, as experiments with fixed H_g collapse onto a single curve, while those with fixed h_0 diverge due to differences in aspect ratio and grain quantity, producing a tilted trend relative to the former. Figure 6(b) presents the scaled maximum wavelength λ/h_0 as a function of Fr_0 for the same dataset. At low Fr_0, buoyant-particle cases generate solitary waves with nearly constant wavelength. As Fr_0 increases, the wavelength grows nonlinearly, with the largest elongation occurring during bore breaking at the highest Fr_0. Comparing particle-laden and particle-free conditions shows that while both exhibit similar wavelengths at low Fr_0, the particle-free case grows more rapidly with increasing Fr_0, reflecting the tendency of clean water to transition to breaking bores at lower Fr_0. Increasing particle size amplifies this discrepancy (see Fig. 5).

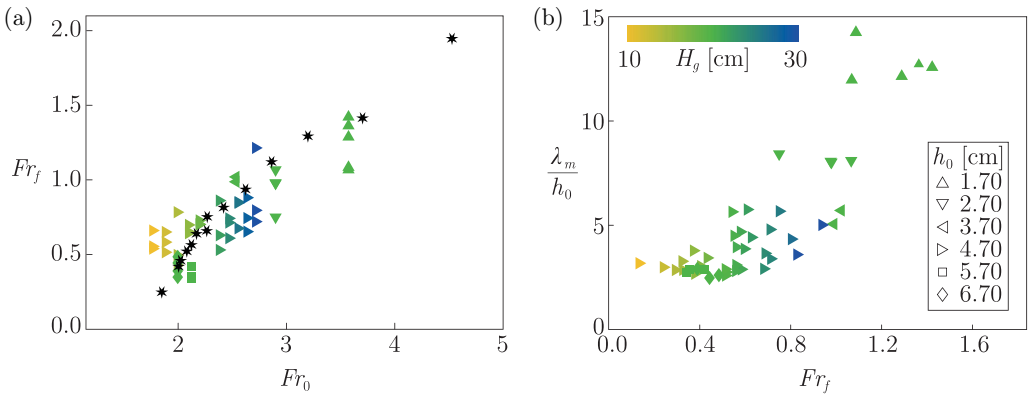

FIG. 7. (a) Local Froude number Fr_f versus global Froude number Fr_0, where marker shape indicates the water depth h_0, color maps to granular column height H_g, and $R = 3.97$ mm. Stars are prior results from Robbe-Saule *et al.* [8] for a particle-free system. (b) Scaled maximum wavelength λ_m/h_0 against Fr_f.

A. Local Froude number Fr_f

An alternative approach for capturing the wave characteristics more accurately is to consider the horizontal velocity of the advancing granular front rather than the vertical velocity of the collapsing grains, expressed through the local Froude number [Eq. (2)] [8]. Figure 7(a) compares the local Froude number Fr_f with the global Froude number Fr_0 for varying granular column height H_g (marker color) and water depth h_0 (marker shape). Seven-pointed stars represent the prior results of Robbe-Saule *et al.* [8]. Although the data follows a trend similar to that observed in particle-free experiments, additional scatter is introduced, suggesting that the correlation between Fr_f and Fr_0 is modestly affected by the presence of buoyant particles. Figure 7(b) shows the scaled maximum wavelength λ_m/h_0 against the local Froude number Fr_0 for varying granular column height and water depth. The data follows a similar trend with Fr_f as it did with Fr_0 [see Fig. 6(b)], but the use of the local Froude number introduces greater variability in the results. Despite this, the analogy of the granular collapse acting as a rigid piston is well suited for developing a predictive model.

B. Wave amplitude model

We next seek a method to predict the wave amplitude directly from the initial conditions of the granular and water columns. To this end, we follow the model formulation proposed by Sarlin *et al.* [23]. Assuming the granular column acts as a horizontal piston for granular collapse, we expect the granular front velocity v_m to scale as $\Delta l/t^*$ where Δl is the granular runout length and t^* is the characteristic spreading time, proportional to $\sqrt{\Delta l/g}$ [46]. Thus,

$$Fr_f = \frac{v_m}{\sqrt{g\,h_0}} \sim \sqrt{\frac{\Delta l}{h_0}}. \tag{3}$$

Figure 8(a) shows A_m/h_0 versus $\Delta l/h_0$ across a range of granular column heights and water depth. The dashed line shows the predicted trend fit to the experimental data: $A_m/h_0 = 0.66\sqrt{\Delta l/h_0}$. The data follows the expected trend for amplitudes as low as $A_m/h_0 \approx 0.45$, where nonlinear transition waves emerge.

To predict the wave amplitude, we first establish a relationship between the measured runout length and the initial conditions of the system. In particular, the final height H_∞ and runout length

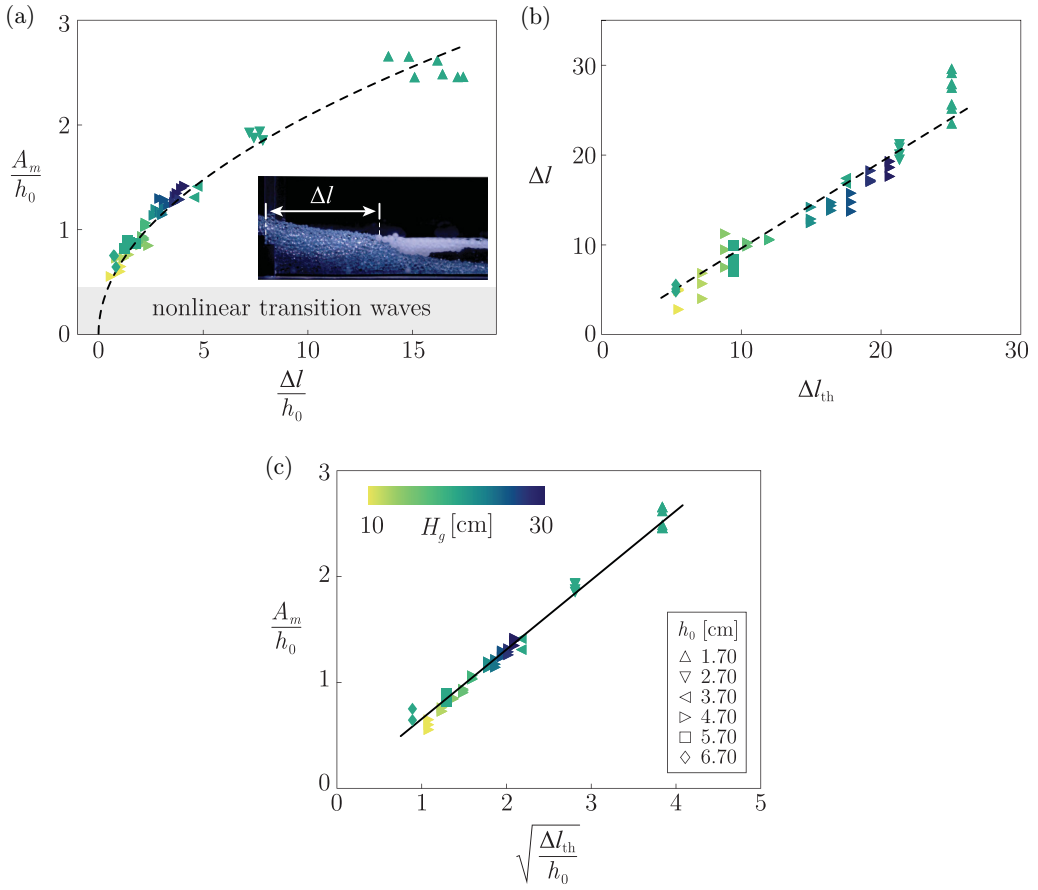

FIG. 8. (a) Nondimensional maximum amplitude A_m/h_0 against scaled runout length $\Delta l/h_0$ with best fit line $A_m/h_0 = 0.66\sqrt{\Delta l/h_0}$. The shaded region indicates nonlinear transition waves $A_m/h_0 \lesssim 0.45$ [23], and the inset shows the runout length for a typical experiment. (b) Runout length Δl against the predicted runout length $\Delta l_{\rm th}$ with best fit line $\Delta l = 0.96\Delta l_{\rm th}$. (c) Maximum scaled amplitude A_m/h_0 against $\sqrt{\Delta l_{\rm th}/h_0}$, where the solid black line is the prediction from Eq. (7). In all plots, the marker color and shape indicate H_g and h_0, respectively, and $R = 3.97$ mm.

$\Delta L_\infty = L_\infty - L_0$ of the collapsed grains must be related to the aspect ratio of the initial granular column. Following Lajeunesse *et al.* [47], this relationship can be expressed as

$$\frac{H_\infty}{L_0} = 0.95\,\alpha^{1/3}, \tag{4}$$

$$\frac{L_\infty}{L_0} = 2.38\,\alpha^{2/3}, \tag{5}$$

which are valid for $\alpha \gtrsim 3$. Assuming the final deposit takes a triangular shape, the predicted runout length at the water surface is $\Delta l_{\rm th} = \Delta L_\infty - h_0 L_\infty/H_\infty$, which, combined with Eqs. (4) and (5), gives

$$\Delta l_{\rm th} = 2.38\alpha^{-1/3}H_0 - \frac{1 + 2.38\alpha^{2/3}}{0.95\alpha^{1/3}}. \tag{6}$$

Figure 8(b) shows the measured runout length Δl against that predicted by Eq. (6). The relationship between the measured and predicted runout length is captured by the trend $\Delta l = 0.96\Delta l_{\text{th}}$. Finally, we can combine Eq. (6) with the empirical fits from Figs. 8(a) and 8(b) to get a prediction for the wave dimensionless wave amplitude:

$$\frac{A_m}{h_0} = 0.65\sqrt{\frac{\Delta l_{\text{th}}}{h_0}}. \tag{7}$$

Figure 8(c) shows that the scaled maximum wave amplitude A_m/h_0 collapses along a single trend when plotted against $(\Delta l/h_0)^{1/2}$, closely following the predicted relationship (black line) from Eq. (7). This demonstrates that the amplitude of a particle-laden wave generated by granular collapse can be predicted using the same framework developed for particle-free surfaces, relying solely on the initial parameters h_0, H_0, and L_0.

VI. DISCUSSION

Our findings demonstrate that buoyant particles can substantially modify impulse waves generated by granular collapse by delaying the transition from non-breaking to breaking waves. This delay alters not only the maximum wave amplitude and wavelength but also the wave's ability to propagate. The effect weakens with particle size, implying that landslides or calving events onto debris-laden water are less likely to produce breaking waves when the floating debris is large—as in coarse ice mélange—compared to finer materials such as grease ice. However, the influence of particle size diminishes rapidly with decreasing surface concentration [36], suggesting that our results represent an upper limit relevant to dense, ice-choked fjords and exceed the effects expected for microplastic-laden ocean surfaces. Similar experiments exploring wave attenuation using buoyant spheres have also reported a decrease in the effect of the buoyant material as surface concentration decreases [38]. The maximum amplitude and wavelength of collapse-driven waves follow the same trends identified in previous studies [8], particularly with respect to the global Froude number Fr_0 and the local Froude number Fr_f. The greater scatter in Fr_f for particle-laden cases indicates that this metric is less reliable when buoyant particles are present. The predictive model of Sarlin *et al.* [23] also describes our data well, requiring only a modest coefficient adjustment from 0.45 to 0.65, likely reflecting differences in bed smoothness that affected the final runout length.

The buoyant particles are themselves influenced by the wave, becoming restructured by both the passing wave and the collapsing granular material. Figure 9 compares waves formed under similar conditions without [Fig. 9(a)] and with [Fig. 9(b)] buoyant particles, with the corresponding movies 4 and 5 are provided [45]. In the absence of particles, the wave surface is highly undulating due to breaking, whereas the particle-laden wave remains smoother. Two distinct regions of elevated particle concentration emerge: a static accumulation adjacent to the collapsed grains and a dynamic region that travels with the wave front. The static buildup buttresses the granular deposit, slightly altering the final runout shape, as evident when comparing image (v) in Figs. 9(a) and 9(b). Similar buttressing effects are observed at glacial fronts in ice-choked fjords, where they impart a resisting force on the glacier terminus [28], influencing seasonal variations in calving behavior [48]. The traveling region beneath the wave evolves as the wave propagates and can locally reach thicknesses comparable to the initial water depth h_0. Near the top of this region, surface transport is enhanced when the waves are near breaking as the particles exhibit a 'surfing' behavior, an effect recently observed in the field by Rainville *et al.* [49]. Alternatively, particles near the base of this region move more slowly than the overlying wave; the particle-laden layer spreads rearward as the wave advances. In natural settings, the buoyant material is typically polydisperse, irregularly shaped, and rougher than the smooth spheres used here, suggesting that both static and dynamic accumulations would be even more pronounced. Understanding how particle shape, size distribution, and surface texture influence these dynamics remains an important direction for future work.

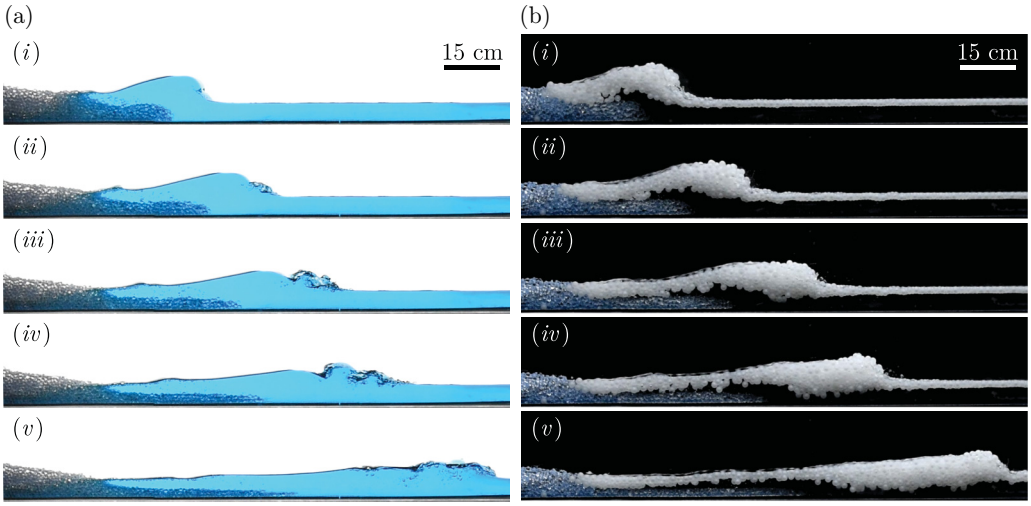

FIG. 9. Image sequence of a breaking wave with (a) no particles, and (b) a monolayer of particles with radius $R = 3.97$ mm as time increases: (i) $t = 0.52$ s, (ii) $t = 0.60$ s, (iii) $t = 0.69$ s, (iv) $t = 0.77$ s, (v) $t = 0.94$ s. The granular column height was $H_g = 17$ cm and $h_0 = 3$ cm.

The coupling between the collapsing granular column, buoyant particles, and generated wave makes these results relevant to several timely applications. For instance, Eq. (7) provides a means of relating wave height to the initial granular configuration, complementing ongoing efforts to connect wave characteristics to their source properties, for example, using tsunami signals recorded by pressure sensors to estimate local calving fluxes [9]. Likewise, the potential impacts of landslide or calving events into particle-laden waters may be evaluated in advance, enabling the implementation of safety measures to protect nearby communities and maritime activity.

VII. CONCLUSIONS

We conducted laboratory experiments on the subaerial collapse of granular columns into water covered by buoyant particles to investigate how floating debris modifies impulse wave generation and propagation. By systematically varying the granular column height, water depth, and particle size, we explored how wave properties and types are affected by each and compared our results to particle-free cases. The buoyant particles were found to delay the transition from nonbreaking to breaking waves, with larger particles exerting a stronger stabilizing influence on the wave front. Despite these differences, the maximum wave amplitude and wavelength scaled primarily with the geometry of the collapsing column, following trends consistent with particle-free surfaces. Moreover, a predictive model derived from the runout dynamics accurately captured the measured wave amplitudes across all conditions, demonstrating that the same geometric framework can be extended to particle-laden surfaces. Together, these findings show that while buoyant surface layers reshape the waveform and particle distribution, the generation of impulse waves remains similar.

Much work remains before conclusions drawn from the simplified physical model explored here can be applied with confidence to real-world scenarios. In particular, the buoyant material used in this study represents an idealized system, and future investigations are needed to determine how particle shape, size distribution, surface roughness, layer thickness, and rigidity influence wave generation. Our results suggest that these properties may drastically alter the resulting wave dynamics, and the experimental framework presented here can be readily extended to such cases and other means of wave generation. For instance, capsizing icebergs have been successfully studied at laboratory scale [17] and are known to generate large water waves [10,31], though the role of

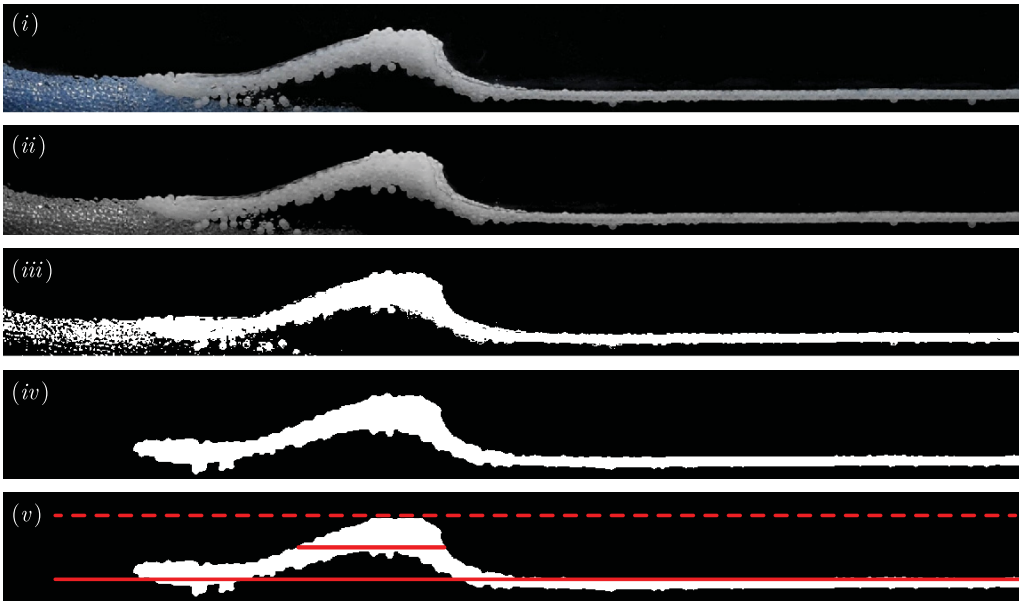

FIG. 10. Processing steps for image analysis: (i) original image, (ii) grayscale image, (iii) binarized image, (iv) filtered binarized image, (v) analyzed image showing locations of interest.

icy, particle-laden water in modulating these waves remains poorly understood. Performing such experiments at reduced scale would provide a systematic means to explore these and other related processes, for which the present findings offer a critical foundation.

ACKNOWLEDGMENTS

This work was supported by the donors of the ACS Petroleum Research Fund under New Directions Grant No. 66804. C.T.G. gratefully acknowledges the Hope Street Fellowship for financial support.

DATA AVAILABILITY

The data that support the findings of this article are openly available [45].

APPENDIX: IMAGE PROCESSING

A custom MATLAB script was developed to isolate the buoyant particle–laden wave generated by the granular collapse. The five-step process is illustrated in Fig. 10. The original image (i) is first converted to grayscale (ii) and then binarized (iii). The binarized frame consists of two distinct white regions: a solid region corresponding to the buoyant particles and a speckled region containing black pixels, which correspond to the glass beads. These regions are separated using close and fill operations (iv). From the resulting image, the wave peak height is identified as the highest white pixel, and the wave amplitude A is defined as the difference between this height and the waterline. The wavelength λ is determined from the distance between the leading and trailing white pixels along the row at the midpoint between the waterline and wave peak (v). The same procedure also enables the separation of the glass bead region from the buoyant particles.

[1] S. T. Grilli, D. R. Tappin, S. Carey, S. F. L. Watt, S. N. Ward, A. R. Grilli, S. L. Engwell, C. Zhang, J. T. Kirby, L. Schambach, and M. Muin, Modelling of the tsunami from the December 22, 2018 lateral collapse of Anak Krakatau volcano in the Sunda Straits, Indonesia, Sci. Rep. **9**, 11946 (2019).
[2] H. M. Fritz, W. H. Hager, and H.-E. Minor, Landslide generated impulse waves. Exp. Fluids **35**, 505 (2003).
[3] L. Rondon, O. Pouliquen, and P. Aussillous, Granular collapse in a fluid: Role of the initial volume fraction, Phys. Fluids **23**, 073301 (2011).
[4] S. Viroulet, A. Sauret, O. Kimmoun, and C. Kharif, Granular collapse into water: Toward tsunami landslides, J. Vis. **16**, 189 (2013).
[5] M. Robbe-Saule, C. Morize, Y. Bertho, A. Sauret, A. Hildenbrand, and P. Gondret, From laboratory experiments to geophysical tsunamis generated by subaerial landslides, Sci. Rep. **11**, 18437 (2021).
[6] S. Viroulet, A. Sauret, and O. Kimmoun, Tsunami generated by a granular collapse down a rough inclined plane, Europhys. Lett. **105**, 34004 (2014).
[7] B. C. McFall and H. M. Fritz, Physical modeling of tsunamis generated by three-dimensional deformable granular landslides on planar and conical island slopes, Proc. R. Soc. A Math. Phys. Eng. Sci. **472**, 20160052 (2016).
[8] M. Robbe-Saule, C. Morize, R. Henaff, Y. Bertho, A. Sauret, and P. Gondret, Experimental investigation of tsunami waves generated by granular collapse into water, J. Fluid Mech. **907**, A11 (2021).
[9] M. Minowa, E. A. Podolskiy, G. Jouvet, Y. Weidmann, D. Sakakibara, S. Tsutaki, R. Genco, and S. Sugiyama, Calving flux estimation from tsunami waves, Earth Planet. Sci. Lett. **515**, 283 (2019).
[10] V. Heller, T. Attili, F. Chen, R. Gabl, and G. Wolters, Large-scale investigation into iceberg-tsunamis generated by various iceberg calving mechanisms, Coast. Eng. **163**, 103745 (2021).
[11] M. M. Das and R. L. Wiegel, Waves generated by horizontal motion of a wall, J. Waterw. Harbors Coast. Eng. Div. **98**, 49 (1972).
[12] T. Jamin, L. Gordillo, G. Ruiz-Chavarría, M. Berhanu, and E. Falcon, Experiments on generation of surface waves by an underwater moving bottom, Proc. R. Soc. A Math. Phys. Eng. Sci. **471**, 20150069 (2015).
[13] W. Sarlin, Z. Niu, A. Sauret, P. Gondret, and C. Morize, Nascent water waves induced by the impulsive motion of a solid wall, J. Fluid Mech. **1008**, A25 (2025).
[14] P. Heinrich, Nonlinear water waves generated by submarine and aerial landslides, J. Waterw. Port Coastal Ocean Eng. **118**, 249 (1992).
[15] G. Sælevik, A. Jensen, and G. Pedersen, Experimental investigation of impact generated tsunami; related to a potential rock slide, Western Norway, Coast. Eng. **56**, 897 (2009).
[16] S. Viroulet, D. Cébron, O. Kimmoun, and C. Kharif, Shallow water waves generated by subaerial solid landslides, Geophys. J. Int. **193**, 747 (2013).
[17] J. C. Burton, J. M. Amundson, D. S. Abbot, A. Boghosian, L. M. Cathles, S. Correa-Legisos, K. N. Darnell, N. Guttenberg, D. M. Holland, and D. R. MacAyeal, Laboratory investigations of iceberg capsize dynamics, energy dissipation and tsunamigenesis, J. Geophys. Res. **117**, 2011JF002055 (2012).
[18] A. Darvenne, S. Viroulet, and L. Lacaze, Physical model of landslide-generated impulse waves: Experimental investigation of the wave-granular flow coupling, J. Geophys. Res. Oceans **129**, e2024JC021145 (2024).
[19] G. Zitti, C. Ancey, M. Postacchini, and M. Brocchini, Impulse waves generated by snow avalanches: Momentum and energy transfer to a water body, J. Geophys. Res. Earth Surf. **121**, 2399 (2016).
[20] F. Mohammed and H. M. Fritz, Physical modeling of tsunamis generated by three-dimensional deformable granular landslides, J. Geophys. Res. Oceans **117**, 2011JC007850 (2012).
[21] W. Sarlin, C. Morize, A. Sauret, and P. Gondret, Nonlinear regimes of tsunami waves generated by a granular collapse, J. Fluid Mech. **919**, R6 (2021).
[22] H. M. Fritz, W. H. Hager, and H.-E. Minor, Near field characteristics of landslide generated impulse waves, J. Waterw. Port Coast. Ocean Eng. **130**, 287 (2004).
[23] W. Sarlin, C. Morize, A. Sauret, and P. Gondret, From granular collapses to shallow water waves: A predictive model for tsunami generation, Phys. Rev. Fluids **7**, 094801 (2022).

[24] L. Lebreton, B. Slat, F. Ferrari, B. Sainte-Rose, J. Aitken, R. Marthouse, S. Hajbane, S. Cunsolo, A. Schwarz, A. Levivier, *et al.*, Evidence that the Great Pacific Garbage Patch is rapidly accumulating plastic, Sci. Rep. **8**, 4666 (2018).
[25] E. A. D'Asaro, A. Y. Shcherbina, J. M. Klymak, J. Molemaker, G. Novelli, C. M. Guigand, A. C. Haza, B. K. Haus, E. H. Ryan, G. A. Jacobs, *et al.*, Ocean convergence and the dispersion of flotsam, Proc. Natl. Acad. Sci. USA **115**, 1162 (2018).
[26] S. E. Bryan, A. G. Cook, J. P. Evans, K. Hebden, L. Hurrey, P. Colls, J. S. Jell, D. Weatherley, and J. Firn, Rapid, long-distance dispersal by pumice rafting, PLoS ONE **7**, e40583 (2012).
[27] J. M. Amundson and J. C. Burton, Quasi-static granular flow of ice mélange, J. Geophys. Res.: Earth Surf. **123**, 2243 (2018).
[28] J. C. Burton, J. M. Amundson, R. Cassotto, C.-C. Kuo, and M. Dennin, Quantifying flow and stress in ice mélange, the world's largest granular material, Proc. Natl. Acad. Sci. USA **115**, 5105 (2018).
[29] D. I. Benn, C. R. Warren, and R. H. Mottram, Calving processes and the dynamics of calving glaciers, Earth Sci. Rev. **82**, 143 (2007).
[30] M. P. Lüthi and A. Vieli, Multi-method observation and analysis of a tsunami caused by glacier calving, Cryosphere **10**, 995 (2016).
[31] F. Chen, V. Heller, and R. Briganti, Numerical modeling of tsunamis generated by iceberg calving validated with large-scale laboratory experiments, Adv. Water Resour. **142**, 103647 (2020).
[32] J. Wolper, M. Gao, M. P. Lüthi, V. Heller, A. Vieli, C. Jiang, and J. Gaume, A glacier–ocean interaction model for tsunami genesis due to iceberg calving, Commun. Earth Environ. **2**, 130 (2021).
[33] D. P. Hoult, Oil spreading on the sea, Annu. Rev. Fluid Mech. **4**, 341 (1972).
[34] S. Martin and P. Kauffman, A field and laboratory study of wave damping by grease ice, J. Glaciol. **27**, 283 (1981).
[35] A. Sauret, F. Boulogne, J. Cappello, E. Dressaire, and H. A. Stone, Damping of liquid sloshing by foams, Phys. Fluids **27**, 022103 (2015).
[36] Y. Sun, T. Bakker, C. Ruf, and Y. Pan, Effects of microplastics and surfactants on surface roughness of water waves, Sci. Rep. **13**, 1978 (2023).
[37] S. Gurusamy, Damping of liquid sloshing by floating balls, Phys. Fluids **35**, 112114 (2023).
[38] R. Calvert, J. Mol, B. R. Sutherland, and T. S. van den Bremer, Attenuation of progressive surface gravity waves by floating spheres, Sci. Rep. **15**, 1770 (2025).
[39] M. E. Cates, J. P. Wittmer, J.-P. Bouchaud, and P. Claudin, Jamming, force chains, and fragile matter, Phys. Rev. Lett. **81**, 1841 (1998).
[40] S. R. Waitukaitis, L. K. Roth, V. Vitelli, and H. M. Jaeger, Dynamic jamming fronts, Europhys. Lett. **102**, 44001 (2013).
[41] I. R. Peters, J. M. Amundson, R. Cassotto, M. Fahnestock, K. N. Darnell, M. Truffer, and W. W. Zhang, Dynamic jamming of iceberg-choked fjords, Geophys. Res. Lett. **42**, 1122 (2015).
[42] A. Levermann, When glacial giants roll over, Nature (London) **472**, 43 (2011).
[43] D. R. MacAyeal, D. S. Abbot, and O. V. Sergienko, Iceberg-capsize tsunamigenesis, Ann. Glaciol. **52**, 51 (2011).
[44] A. Gans, A. Abramian, P.-Y. Lagrée, M. Gong, A. Sauret, O. Pouliquen, and M. Nicolas, Collapse of a cohesive granular column, J. Fluid Mech. **959**, A41 (2023).
[45] N. Reyner, C.T. Gabbard, and J.B. Bostwick, Granular collapse on particle-laden water, Github repository (2025), https://github.com/chase-gabbard/BuoyantWaterWave.
[46] W. Sarlin, C. Morize, A. Sauret, and P. Gondret, Collapse dynamics of dry granular columns: From free-fall to quasistatic flow, Phys. Rev. E **104**, 064904 (2021).
[47] E. Lajeunesse, J. B. Monnier, and G. M. Homsy, Granular slumping on a horizontal surface, Phys. Fluids **17**, 103302 (2005).
[48] Y. Meng, C.-Y. Lai, R. Culberg, M. G. Shahin, L. A. Stearns, J. C Burton, and K. Nissanka, Seasonal changes of mélange thickness coincide with Greenland calving dynamics, Nat. Commun. **16**, 573 (2025).
[49] E. J. Rainville, J. Thomson, M. Moulton, and M. Derakhti, Surfing transport of buoyant objects observed in the nearshore, J. Geophys. Res. Oceans **131**, e2025JC022422 (2026).